Texture Mapping for 3D Reconstruction with RGB-D Sensor

Yanping Fu[1] Qingan Yan[2] Long Yang[3] Jie Liao[1] Chunxia Xiao[1]
[1] School of Computer, Wuhan University, China
[2] JD.com
[3] College of Information Engineering, Northwest A&F University, China
{ypfu,liaojie,cxxiao}@whu.edu.cn, qingan.yan@jd.com, yl@nwsuaf.edu.cn

Abstract

Acquiring realistic texture details for 3D models is important in 3D reconstruction. However, the existence of geometric errors, caused by noisy RGB-D sensor data, always makes the color images cannot be accurately aligned onto reconstructed 3D models. In this paper, we propose a global-to-local correction strategy to obtain more desired texture mapping results. Our algorithm first adaptively selects an optimal image for each face of the 3D model, which can effectively remove blurring and ghost artifacts produced by multiple image blending. We then adopt a non-rigid global-to-local correction step to reduce the seaming effect between textures. This can effectively compensate for the texture and the geometric misalignment caused by camera pose drift and geometric errors. We evaluate the proposed algorithm in a range of complex scenes and demonstrate its effective performance in generating seamless high fidelity textures for 3D models.

1. Introduction

With the emergence of RGB-D sensors, 3D reconstruction has made significant progress in recent years. While both small-scale objects and large-scale scenes can be modeled with impressive geometric details [10, 17, 26, 27, 28], the recovered texture fidelity for 3D models is still less satisfactory [7, 13, 22].

Why does texture mapping technology lag so behind 3D modeling? The reasons are fourfold: 1) Due to the noise of depth data, reconstructed 3D models always accompany geometric errors and distortions. 2) In camera trajectory estimation, the pose residual would be gradually accumulated and lead to camera drift. 3) The timestamp between captured depth frame and color frame is not completely synchronized. 4) RGB-D sensors are usually in low resolution, and the color image is also vulnerable to light and motion conditions. All of the challenges above contribute to the produce of misalignments between geometric models and corresponding images and lead to undesired mapping results.

While projective mapping methods [21, 23] can reduce blurring and ghosting artifacts caused by multi-image blending, the texture bleeding is unavoidable on the boundary of different views, due to geometric registration errors and camera trajectory drift. Zhou and Koltun [30] propose an optimization framework using local image warping, which can compensate for geometric misalignments. However, this method needs to subdivide the mesh model, which will greatly increases the amount of data and limit its application scope. Furthermore, the weighted average strategy which is usually adopted in multi-image blending is sensitive to the light change and motion blur cased by fast camera movement.

To overcome the challenges, in this paper we propose a novel texture mapping method which performs a global-to-local non-rigid correction optimization. First, we choose an optimal image for each face to avoid the artificial effects in multi-image blending. In the global optimization step, we use a unified color consistency and geometry consistency optimization to rectify the camera pose of each texture block from different views. Then in the local optimization step, we find an additional transformation for boundary vertices of the block to refine the texture coordinate drift caused by geometric errors. Finally, we adopt the texture atlases to map the texture onto desired 3D model.

We validate the effectiveness of the proposed method in a range of complex scenes and show high fidelity textures. In contrast to the method [30], our method is much faster and needs much less triangle information. The texture blurring artifacts are also greatly eliminated. As compared to [23], our method can effectively reduce the seam inconsistency between face boundaries and is tolerant of geometric misalignments.

2. Related Work

Texture mapping is an important step for acquiring realistic 3D models [11, 16, 26, 29]. In this section, we revisit

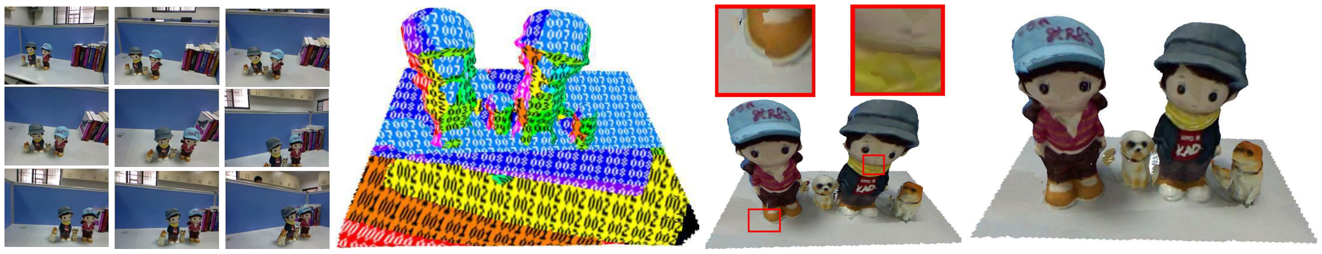

(a) Input (b) View image selection (c) Global optimization (d) Global + local optimization

Figure 1: The overview of the proposed approach. (a) The input images for texture mapping. (b) The selected optimal texture image for each face. The numbers with different colors indicate the selected image indexes. (c) The result using only global optimization. (d) The result of global-to-local optimization.

some kinds of related approaches that aim at improving the effect of texture mapping.

Blending-based methods: A commonly used way for texture mapping is to blend multiple images into textures [3, 8, 20] adopting different weighted average strategies. Current RGB-D reconstruction systems [25, 19, 7] mainly rely on the truncated signed distance function (TSDF) representation. That means, they need to add an additional color volumetric grid, besides TSDF volumetric grid, to compute the color of each vertex by running weighted average of multiple images. However, this makes such kind of methods sensitive to computational noises; the blurring and ghosting would easily emerge if the recovered camera pose or 3D geometry is slightly inaccurate. Moreover, the process of model subdivision and the variety of model size in different viewpoints also affect their performance.

Projection-based methods: Another mechanism is projective texture mapping, which associates each face or vertex with one appropriate image. Lempitsky et al. [21] use the pairwise Markov Random Field to select an optimal image for each face. Inspired by this work, Allene et al. [2] and Gal et al. [14] introduce additional metrics to improve the data term and smooth term for selecting more appropriate views. However, these methods face a challenging issue, that is, how to mitigate the visual seams between adjacent face textures. To overcome the problem, they have to additionally add a post-process by respectively utilizing multi-band blending [6] and poisson editing [15]. Waechter et al. [23] propose a global color adjustment algorithm to diminish the visual fracture caused by view projection. While these methods can greatly reduce blurring and ghosting artifacts caused by multi-image blending, the texture bleeding is unavoidable on the boundary of different views, due to geometric registration errors and camera trajectory drift.

Warping-based methods: Different from above approaches, warping-based methods have more resistance to the misalignment problem caused by geometric errors and camera drift. Eisemann et al. [12] introduce a local texture warping method by estimating the optical flow between projected texture images. Aganj et al. [1] apply different deformations to different images in order to fit the recovered mesh. The displacement field is computed by matching feature points in different views through a thin-plate spline approximation. Furthermore, Zhou and Koltun [30] design a texture mapping framework where both camera poses and geometric errors are rectified via local image warping. However, this method needs to subdivide the mesh model, which will greatly increase the amount of data and limit its application scope. Moreover, these methods also suffer from blurring artifacts as weighted average blending strategies are still utilized. More recently, Bi et al. [4] use patch-based synthesis to generate a new target texture image for each face to compensate for the camera drift and reconstruction errors, but the scenes containing dynamic shadows will be a challenge to this method.

3. Overview

The goal of this work is to map texture images onto 3D models which are acquired by a commodity depth camera. The input is a RGB-D sequence or live video that contains depth frames and corresponding color frames, and the output is a 3D model accompanying high fidelity textures. To achieve this goal and overcome the aforementioned challenges, we propose a global-to-local optimization strategy which contains four main steps. Fig. 1 shows the overview of the proposed approach.

Input: The input of our algorithm is a RGB-D sequence or live video acquired by Kinect V1. For more detailed color information, it is also recommended to add an additional HD camera on top of the Kinect to obtain high resolution texture images. However, in justice to comparison, we still adopt the low resolution color image of Kinect V1 as input in experiments.

Preprocess: A mesh model is reconstructed from the input depth sequence as initial model M_0 for texture mapping, and a subset of frames is extracted from the original color sequence as texture candidates. To improve the quality and reduce computation complexity, unlike [30], we utilize [28] to reconstruct 3D models instead of KinectFusion [18, 22], and select texture candidate images by weighting the elements of image clarity, jitter, blur and viewport overlay. This step produce an initial model M_0 and a set of camera poses $\{\mathbf{T}_i^0\}$ corresponding to the selected color image subsequence $\{\mathbf{C}_i\}$ and depth image subsequence $\{\mathbf{D}_i\}$.

Optimization: To construct high fidelity texture, our approach combines the advantages of [23] and [30]. We select an optimal texture image for each face of the model to avoid the blurring caused by multi-image blending. Thus by regarding each candidate image as a label, we formulate the selection problem into a multi-label Markov field in company with the angle between camera poses and normal map, projection area and the distance from model face to camera plane. However, because both $\mathbf{T}^0$ and M_0 are not absolutely accurate, adjacent faces with different labels usually can not be completely stitched. To solve this problem, we adopt a global-to-local optimization strategy. For global optimization, we adjust the camera pose of each texture block based on the color consistency and geometric consistency between relevant blocks. In local optimization stage, we import an additional transformation to refine texture coordinates on the boundary of the different blocks and make seamlessly stitched textures.

Texture Atlases: Finally, we utilize texture atlases to map the desired texture onto 3D models. Each face is projected onto its associated texture image, under optimized camera pose, to get projection region. Every projected region is used to establish the texture atlases, while recording the vertex coordinate of each triangle face. We then transform them into atlases space. In this way, the texture of each vertex can be directly retrieved in atlases via texture coordinates, and generate the final textured model.

4. Texture Mapping Method

In this section we will elaborate on each step in more detail. Let M_0 represent the reconstructed mesh model for texture mapping, $\{\mathbf{v}_i\}$ and $\{\mathbf{f}_i\}$ are respectively the vertex set and the face set of M_0, where each face represents a triangle mesh on the model. $\mathbf{T}$ is a 4×4 transformation matrix, which transforms the vertex $\mathbf{v}_i$ of M_0 from world coordinates to local camera coordinates, as defined by:

$$\mathbf{T} = \begin{bmatrix} \mathbf{R} & \mathbf{t} \\ \mathbf{0} & 1 \end{bmatrix}, \quad (1)$$

where $\mathbf{R}$ is the 3×3 rotate matrix and $\mathbf{t}$ is the 3×1 translation vector.

We also specify the perspective projection of a 3D vertex $\mathbf{v} = [x, y, z]^T$ onto 2D image plane as Π. Thus the pixel coordinate $\mathbf{u}(u, v)$ for the vertex $\mathbf{v}$ on the image plane can be computed through:

$$\mathbf{u}(u, v)) = \Pi(\mathbf{K}\mathbf{v}) = (\frac{xf_x}{z} + c_x, \frac{yf_y}{z} + c_y)^T, \quad (2)$$

where $\mathbf{K}$ is the camera intrinsic matrix, f_x, f_y are the focal lengths, and c_x, c_y correspond to the coordinate of the camera center in pinhole camera model. Furthermore, we use $\mathbf{D}$ representing depth image, $\mathbf{C}$ denoting color image and I corresponding to the intensity of color image.

4.1. Model Reconstruction

The input of our pipeline is a stream of depth images and an accompanying RGB color sequence. In our system, we make use of Microsoft Kinect V1 to capture these data. As the input frames of Kinect V1 are in low resolution and would be easily influenced by motion blur and jitter effect, we thus select a subset of high confidence frames for scene modeling and texture mapping.

Our method utilize the sparse-sequence fusion (SSF) method [28], instead of KinectFusion [18, 22], to reconstruct the initial 3D model and extract high confidence color frames. This method takes account of the jitter, blur and some other factors that contribute to noises in scanning. It can reconstruct a mesh model M_0 with a sparse depth image sequence $\{\mathbf{D}_i\}$. The basic function of [28] is defined as follows:

$$E_{ssf} = \lambda_1 E_{jit}(i) + \lambda_2 E_{dif}(i) + \lambda_3 E_{vel}(i) + E_{sel}(i), \quad (3)$$

where $E_{sel}(i)$ is a switch term controls the selection of depth image $\mathbf{D}_i$. It should be set to 1 if current image is considered as valid image to be integrated, otherwise it takes 0. $E_{jit}(i)$ measures the jittering effect via calculating the instant viewpoint change between selected images. The continuity term $E_{dif}(i)$ is to ensure sufficient scene overlap between two selected supporting images by accumulating camera pose change, and $E_{vel}(i)$ evaluates the camera motion velocity. Besides of these elements, in order to get high clarity images, we additionally import a term to depict the quality of each color frame. Eq. 4 shows our objective function for frame extraction:

$$E(i) = E_{ssf}(i) + \lambda_{cla} E_{cla}(i), \quad (4)$$

where E_{ssf} is the SSF term and λ_{cla} is a balance parameter. We use $\lambda_{cla} = 10$ in our experiments, and the others are set in accordance with [28]. Clarity term E_{cla} is defined as:

$$E_{cla}(i) = \begin{cases} exp^{\theta_i} - 1, & if\ E_{sel} == 1 \\ 0. & if\ E_{sel} == 0 \end{cases} \quad (5)$$

The blurriness value θ is calculated via [9]. Eq. 5 shows that once the depth image $\mathbf{D}_i$ is added into the supporting subset, the clarity of its corresponding color image $\mathbf{C}_i$ has to be calculated; otherwise, ignored directly, according to the value of $E_{sel}(i)$. The iteration proceeds until all captured images have been processed. This will produce a sparse color image sequence $\{\mathbf{C}_i\}$ with associate camera poses $\{\mathbf{T}_i^0\}$, which can be used as the texture candidates.

4.2. Texture Image Selection

Many texture mapping methods [3, 8, 20] project mesh onto multiple image planes, and then adopt weighted average blending strategy to synthesize model textures from pixels [11, 16]. They ideally assume that the estimated geometry surfaces and camera poses are enough accurate, however in practice, this would be easily violated. Therefore, instead of directly synthesizing from multiple images, we respectively select an optimal texture image for each face of the model M_0. By regarding each candidate image as a label, we formulate this selection problem into a pairwise Markov Random Field (MRF) based on [2]:

$$E(\mathbf{C}) = E_d(\mathbf{C}) + \lambda E_s(\mathbf{C}). \quad (6)$$

The data term E_d projects each model face onto each candidate image $\mathbf{C}_i$ and measure the area of projection region, which is related to the angle view proximity, angle, image resolution, and visibility constraint, as defined by:

$$E_d(\mathbf{C}) = -\sum_{i}^{\{\mathbf{C}_i\}} \sum_{j}^{\{\mathbf{f}_j\}} area[\Pi_{\mathbf{C}_i}(\mathbf{f}_j)]. \quad (7)$$

The smooth term E_s, described by Eq. 8, calculates the integral along edge e to measures color differences, where e is the common edge between adjacent faces assigned to different texture images $(\mathbf{C}_i, \mathbf{C}_j)$. ε is the entire edge set of the model M_0.

$$E_s(\mathbf{C}) = \sum_{e_{ij} \in \varepsilon} \int_e \left\| I_{\mathbf{C}_i}(\Pi_{\mathbf{C}_i}(x)) - I_{\mathbf{C}_j}(\Pi_{\mathbf{C}_j}(x)) \right\| dx. \quad (8)$$

The MRF function $E(\mathbf{C})$ of Eq. 6 is minimized with graph cuts and alpha expansion [5].

4.3. Global Optimization

The above step associates each face with an texture image $\mathbf{C}_i$. However, due to the existence of geometry error and camera drift, directly using texture stitching or color adjustment post-processing [21, 14] cannot make the textures on adjacent faces visually consistent. This is the main challenge for projective texture mapping methods. To eliminate visual seams, we draw upon the idea of non-grid correction to stitch textures between adjacent faces.

Through extrinsic matrix $\mathbf{T}^0$ and intrinsic matrix $\mathbf{K}$, model faces can be easily projected to their associate images to obtain texture colors. Yet matrix $\{\mathbf{T}_i^0\}$ are always noisy,

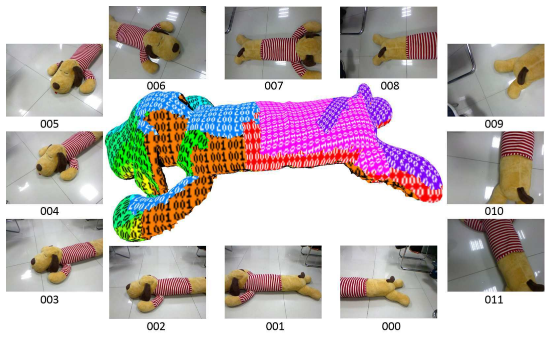

Figure 2: Clustering the model faces according to their texture images.

so that the texture colors obtained through these transformations may be also inaccurate. In this section, we thus have to optimize $\{\mathbf{T}_i^0\}$ to make sure that all the faces coming from different texture images can be closely aligned.

We first perform a face clustering process based on texture image $\{\mathbf{C}_i\}$, that is, if two adjacent faces correspond to the same texture image, we put them together in the same labeled cluster. After traversing all faces, a collection of clusters can be obtained, as shown in Fig. 2 with different colors. For the sake of clarity, we name that the all faces within the same cluster as a *chart*. In order to improve robustness, if the number of faces F_i in a chart i is less than a threshold F_N, this chart will be merged into its closest neighbor j, which is measured by three elements: 1) The viewpoint angle between texture images of chart i and j should be minimal. 2) The number of faces meets the criteria of $F_j > F_N$. 3) The projection of all vertices in chart i onto the texture image of chart j should still stay in bounds. We empirically set $F_N = 50$ in our subsequent experiments. Based on the clusters, we establish an undirected connection graph $\mathbf{G}$ from the charts; if two charts are adjacent to each other, there will be an edge $g_{ij} \in \mathbf{G}$ linking them.

The texture for faces in the chart comes from the same image, so they are well aligned. That means, in order to generate a natural texture for the model, we only need to adjust the textures between different charts. For ideal texture mapping, we believe that the boundary texture of one chart can be totally recovered by the texture of its adjacent charts. Based on this observation, we can align adjacent chart textures as long as it is possible to minimize the inconsistency between associated texture and projected texture of each chart and its neighbors. However, only considering the color consistency may lead to misalignment in texture-less regions. Therefore, we additionally take the geometric consistency into consideration, which serves as a regular term in Eq. 9. We formulate our objective function as follows by measuring both color consistency and geometric consistency for each chart:

$$E(\mathbf{T}) = \sum_{i}^{chartN} \sum_{j\in\mathbf{G}_i} \sum_{k\in chart_i}^{N} (I_i(\Pi(\mathbf{T}_i\mathbf{v}_k) - I_j(\Pi(\mathbf{T}_j\mathbf{v}_k)))^2 + \lambda_{depth} \sum_{i}^{chartN} \sum_{k\in chart_i}^{N} (\varphi(\mathbf{T}_i\mathbf{v}_k) - D_i(\Pi(\mathbf{T}_i\mathbf{v}_k)))^2 , \tag{9}$$

where $\mathbf{v}_k$ denotes the whole vertex set in chart i and N is its number. $chartN$ represents the number of chart on model M_0. Function $\varphi(\mathbf{x})$ computes the Z component of the vector $\mathbf{x}$. $\mathbf{G}_i$ depicts the neighborhood of chart i. The first term makes the texture of chart i consistent with the projected texture of its adjacent chart j. The second term ensure that, when $\mathbf{T}$ changes, the optimized camera pose not only makes the texture consistent, but also the reconstructed model to be consistent with the depth image acquired by RGB-D camera, and ensure the camera pose $\mathbf{T}$ not to deviate far apart from the initial value $\mathbf{T}_0$ when the color constraint is insufficient. By minimizing the Eq. 9, we can compute a correction transformation matrix for each chart, which makes the adjacent charts closer to each other and reduces visual seams.

4.4. Local Optimization

While the global optimization is able to make most textural regions stitched, for some areas with large geometric errors (as shown in the red box of Fig. 1(c)), the textures still could not be accurately aligned. The global optimization can only correct the camera drift of each chart. If the reconstructed geometric model is accurate enough, all textures will be well stitched after the global optimization. Unfortunately, the ubiquity of geometry errors makes the only global optimization is insufficient for high fidelity texture mapping. Thus we introduce a further adjustment on each face of the model so that local textures can be also well aligned.

Because all faces on one chart correspond to the same texture image, there is therefore no need to optimize the entire chart. In addition, as each chart has been roughly aligned in the global optimization step, it is only necessary to perform correcting on a small set of vertices to make up for texture misalignment caused by geometric errors. Instead of editing the mesh model, we propose to warp the projected coordinates of boundary vertices in each chart. As shown in Fig. 3(b), in order to align the texture at vertex v, we can move the projected coordinate of v in image A to align the texture of v in image B. As long as the boundary vertices are optimized, the texture of whole chart will be well aligned.

However, moving the projection coordinate of a vertex is a ill-posed problem. To address the challenge, we find

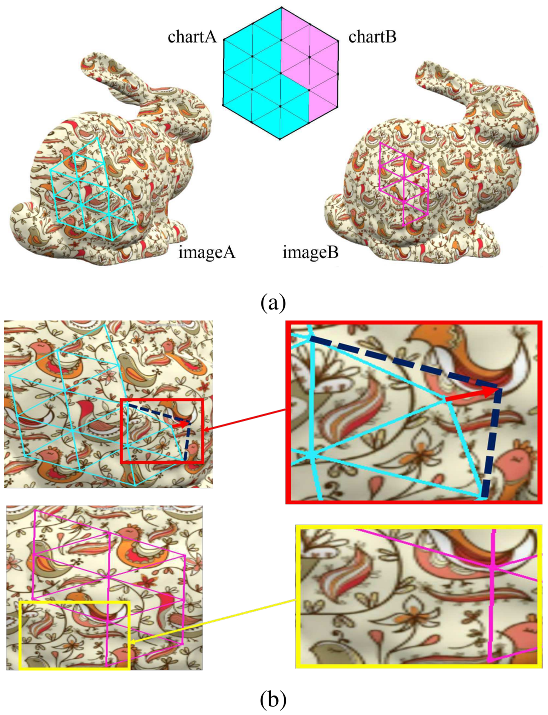

Figure 3: (a) The projection area of two adjacent charts onto their respective texture images. (b) Correcting the texture coordinate of the vertex v in chart A makes it align to the coordinate of vertex v in the texture image of chart B.

an optimal moving vector for the texture coordinate of each boundary vertex and make it aligned with its adjacent chart textures. To this end, we compute an additional transformation matrix for the vertex v on the boundary of chart instead of calculating the moving vector directly. The additional transformation ensures that the chart where the vertex v is located is sufficiently aligned with the charts connected to v. Then we use this matrix to obtain the optimal projection coordinate for v as texture coordinate. The texture coordinate correction process is able to make the local texture at each boundary vertex v to be sufficiently aligned. We design an objective function to compute this matrix of v to correct texture coordinate in the image as follows:

$$E(\mathbf{T}_{ij}) = \sum_{i}^{chartN} \sum_{j}^{vertN} \sum_{k}^{adjN} (I_i(\Pi(\mathbf{T}_{ij}\mathbf{T}_i\mathbf{v}_j))) - I_k(\Pi(\mathbf{T}_{kj}\mathbf{T}_k\mathbf{v}_j)))^2 + \lambda_{reg} \sum_{i}^{chartN} \sum_{j}^{vertN} (\mathbf{T}_{ij}^T\mathbf{T}_{ij} - \mathbf{I}) , \tag{10}$$

where j represents the boundary vertex of chart i, k represents the adjacent charts of i which share vertex j and $\mathbf{v}$ represents the whole vertices in chart i. $\mathbf{T}_{ij}$ is an additional

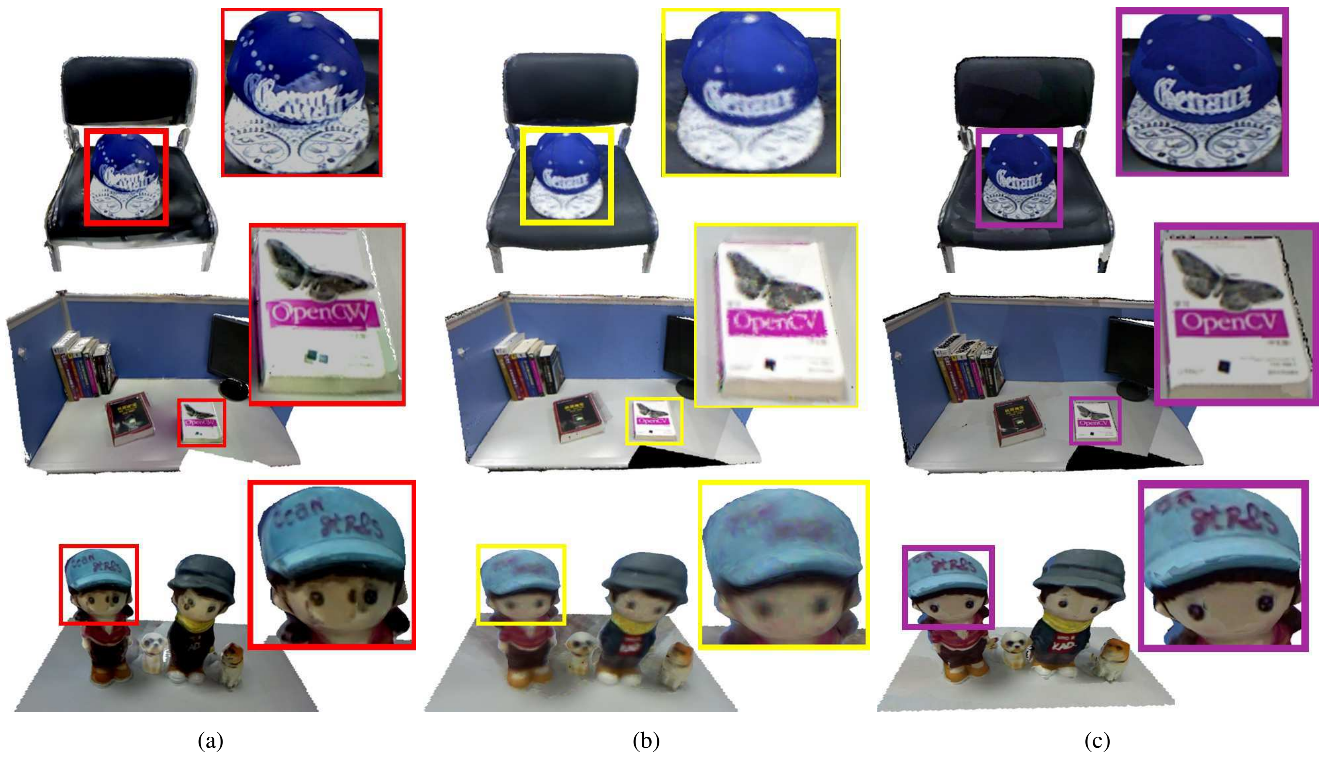
Figure 4: Comparisons with the state-of-the-art algorithms of [23] and [30]. (a) The results generated by [23]. (b) The results produced by [30]. (c) The mapping results of our method.

transformation matrix used to correct the texture coordinate of vertex j, which make projection texture of vertex j in chart i consistent with the projected texture on texture image of the adjacent chart k. $\mathbf{T}_i$ and $\mathbf{T}_j$ are the transform matrix optimized by global optimization for chart A and chart B. $\mathbf{I}$ represents the identity matrix. The first item is data term, which makes the texture of the vertex on the boundary of chart as aligned as possible. The second item is regular term, it ensure that the additional matrix is not deviate from the result of global optimization.

We use the Gaussian Newton iteration to solve Eq. 9 and Eq. 10. We get the camera transformation $\mathbf{T}_i$ for each chart after the global optimization. For a vertex on the boundary of chart, we obtain an additional transformation to correct the projected texture coordinate, which can make the texture align to the texture of adjacent faces at this vertex. Then we repeat the process until all the boundary texture coordinates are processed.

The entire chart can be projected via $\mathbf{T}_i$ to the texture image to get the texture coordinates, for the vertices on boundary of the chart we further use a transformation $\mathbf{T}_{ij}$ for non-rigid correction to get corrected texture coordinates. We save the texture coordinates and obtain the texture atlases. Finally, using texture atlases technology, we can generate a seamless texture model.

5. Results

We evaluate the proposed approach on four datasets, which are acquired by Microsoft Kinect V1 sensor. All experiments were performed on a computer with Intel Core i7 3.6 GHz CPU, 8 GB of RAM, and NVIDIA GeForce GTX 1060 6 GB. The parameters $\lambda_{depth} = 2$ and $\lambda_{reg} = 10$ are used in our experiments. We validate the performance of the proposed method by mainly comparing with the state-of-the-art approaches [23] and [30]. We directly use the code provided by the authors of [23] and implement a version of [30] by ourselves. The experiments show the outperformance of our method, especially in challenging lighting and shadow conditions.

Fig. 4 shows the comparison results of these three methods in different scenes. Because of the limited frame resolution of Kinect V1, the reconstructed models miss a lot of geometric details. In addition, low quality of color images also lead to the absence of texture information, which causes a big challenge for texture mapping. Our method fully takes advantage of the available image context on both global and local layers. The global optimization tries to make the textures coming from different charts aligned as much as possible. In local layer, boundary textures are refined through a texture coordinate correction. As illustrated in Fig. 4(c), even though the doll is only $25cm$ high, our

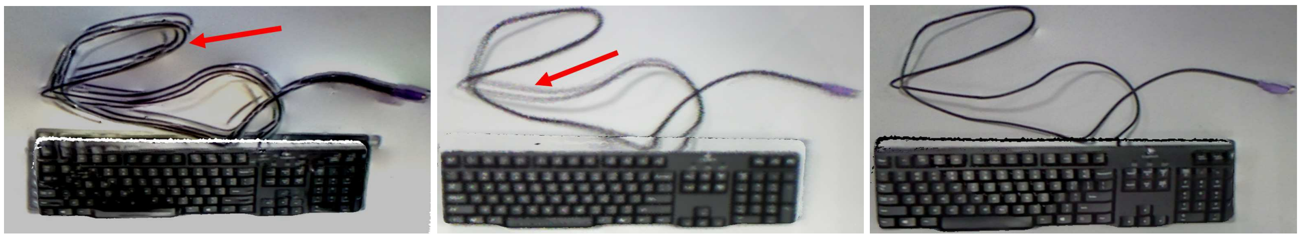
(a) (b) (c)

Figure 5: Texture mapping results in the scene with shadows. The area indicated by red arrow shows the error caused by shadow. (a) The result of [23]. (b) The result generated by [30]. (c) Our texture mapping result.

	scene information			running time (s)					
model	points	faces	key frames	T_s	T_g	T_l	T_t	[23]	[30]
toy	40705	79682	14	1.087	16.591	4.446	27.608	147.068	341.755
book	178584	352510	16	2.262	84.792	57.053	157.014	486.649	902.207
hat	70623	137767	10	2.475	29.193	13.263	59.949	214.774	1002.190
keyboard	68238	134475	13	4.223	26.478	7.594	47.637	321.973	1513.080

Table 1: The performance statistics of [23], [30] and our algorithm. The running time of global optimization and local optimization of our method is recorded through 30 iterations and 10 iterations respectively. T_s, T_g and T_l respectively denote the computational time required by view selection, global optimization and local optimization. T_t is the total process time of our algorithm. The timings of [30] is recorded under 30 iterations.

method is still able to produce more faithful mapping results than the other approaches; the texture is very closer to the original content of input images and contain rarely blurring and seaming artifacts. As [23] cannot overcome the disturbance of geometric and camera drift, the mapping result generated by this approach contains obvious misalignment errors and texture seams. On the other hand, the weighted averaging strategy adopted in [30] makes it suffer from blur effects. This will become even more serious when the color image resolution is low. Even with the help of local warping process, the texture is still blurred as shown in Fig. 4(b).

Table 1 shows the performance statistics of the proposed algorithm, including point, face and key frame numbers, the running time of each step in our method and timings requested by [23] and [30]. To be fair, all methods share the same model and keyframe sequences and iteration number. While [23] does not optimize the geometric errors and camera drift, it spends more time on global color correction and local color stitching. We also found that the method of [30] not only correct the camera drift and geometric distortion, but also subdivide the grid of 3D model, which increases the amount of processing data and requires more time than ours.

Fig. 5 shows the comparison results in a challenging shadow scene. The shadows are produced by multiple lights, and the shadow position and shape vary in different views. In Fig. 5(c), it is notable that our method can produce much clearer result than the others, for example, the texture beside of the keyboard cable. In our approach, the texture information of shadow regions are selected from the same texture image or similar viewpoint images, which can effectively avoid the influence of position and shape differences in different views. In contrast, [23] incorrectly generates multiple cable textures beside the keyboard, as they only consider color consistency and correct the texture without considering the depth constraints. The results of [30] suffer from blurring issue; the texture color is diluted by neighboring pixels. Although it uses local warping to further correct the texture, due to the difference of shadow shape in multiple images, the blur inevitably occur after using weighted average. We also evaluate our algorithm in some challenging scenes with sparse and sharp texture details, as shown in Fig. 6. The first row shows a box with sharp shape patterns and small characters. The other is a chair covered with a sparse-flower style cushion. Due to its sparseness in texture and lack of geometric details, [23] and [30] produce seriously ghosting and blurring artifacts on these datasets.

Furthermore, to illustrate the effect of each step in our proposed global-to-local optimization framework, we give the comparison between only using global optimization and joint global and local process. As shown in Fig. 7(a), using only global optimization, while the texture can be basically alignment, visual seams are still existed in the areas with large geometric errors; yet the local optimization can great-

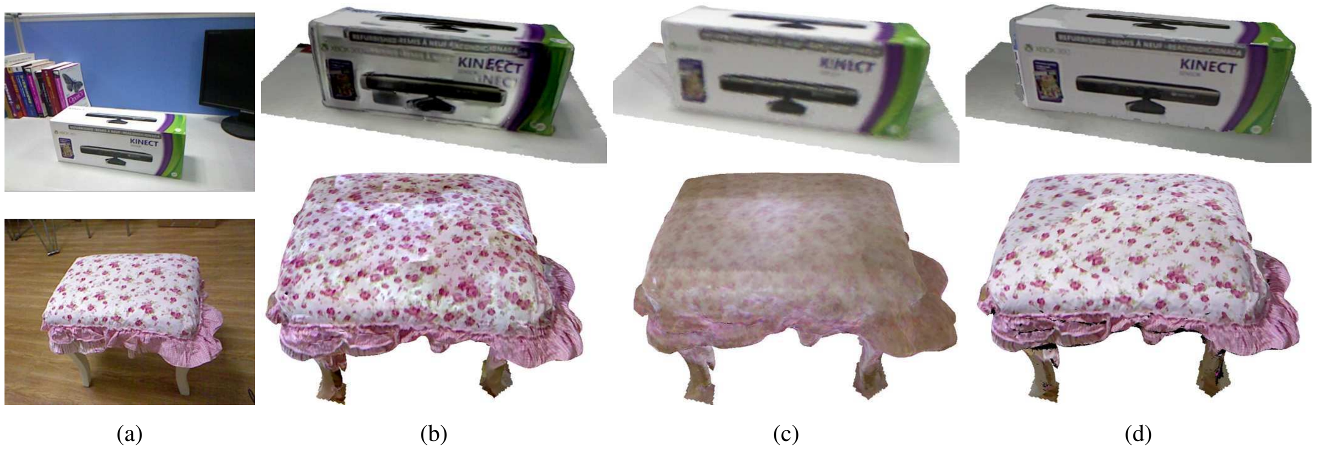

Figure 6: Comparisons on challenging datasets with sparse and sharp texture details. (a) The input image. (b) The results reconstructed by [23]. (c) The results reconstructed by [30]. (d) The results reconstructed by our method.

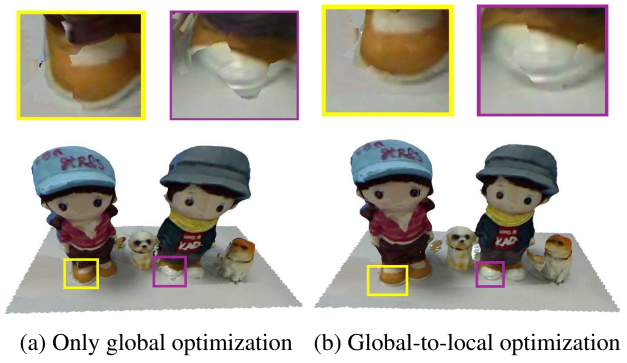

Figure 7: The results of using only global optimization and joint global-to-local optimization.

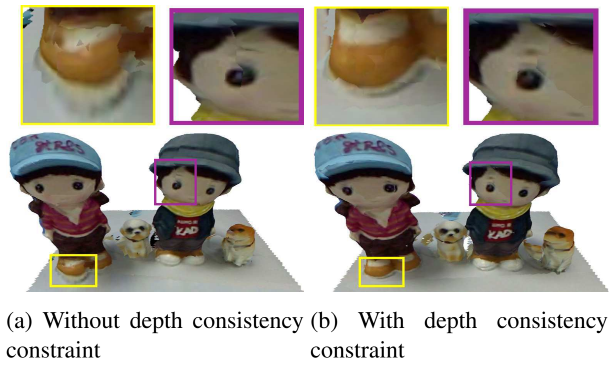

Figure 8: The results of using depth consistency constraint and without depth consistency constraint.

ly reduce these artifacts as in Fig. 7(b).

Fig. 8 shows the reason why we import the depth consistency constraint into our global optimization. The regions around shoes and eyes are misaligned, due to the lack of texture variety. This can not be solved only using color consistency, but in depth image the information is rich. As shown in Fig. 8(b), the texture can be aligned well after further using the depth consistency constrain.

Limitation: Our method also suffers from two limitations. Local optimization requires adding an affine transformation to the texture area, yet the texture may be stretched and shrunk on the boundary of charts. When geometric error is large, the correction would still generate some local texture distortions to final mapping results. Moreover, the lack of sufficient geometric details also increases the challenges in face clustering and texture sitching.

6. Conclusion

In this paper, we have proposed a non-rigid texture mapping method for 3D models reconstructed by an RGB-D sensor. The input of our method is an RGB-D video sequence, and the output is a 3D reconstruction model with high quality texture. We introduce a global optimization step to adjust texture positions, and design a local optimization to further refine texture boundaries. The experiments show that our method can produce high fidelity texture models in even challenging scenes. In the future, we would like to import the visual saliency information [24] into our framework for more detailed texture recovery.

Acknowledgments This work was partly supported by The National Key Research and Development Program of China (2017YFB1002600), the NSFC (No. 61472288, 61672390), Foundation of Key Research Institute of Humanities and Social Science at Universities (16JJD870002), Chinese Ministry of Education, Wuhan Science and Technology Plan Project (No. 2017010201010109). Chunxia Xiao is the corresponding author.

References

[1] E. Aganj, P. Monasse, and R. Keriven. Multi-view texturing of imprecise mesh. In *Asian Conference on Computer Vision*, pages 468–476, 2009.

[2] C. Allene, J. P. Pons, and R. Keriven. Seamless image-based texture atlases using multi-band blending. In *International Conference on Pattern Recognition*, pages 1–4, 2008.

[3] F. Bernardini, I. M. Martin, and H. Rushmeier. High-quality texture reconstruction from multiple scans. *Visualization & Computer Graphics IEEE Transactions on*, 7(4):318–332, 2001.

[4] S. Bi, N. K. Kalantari, and R. Ramamoorthi. Patch-based optimization for image-based texture mapping. *ACM Transactions on Graphics*, 36(4), 2017.

[5] Y. Boykov, O. Veksler, and R. Zabih. Fast approximate energy minimization via graph cuts. *IEEE Transactions on Pattern Analysis and Machine Intelligence*, 23:2001, 2001.

[6] P. J. Burt and E. H. Adelson. A multiresolution spline with application to image mosaics. *ACM Trans. Graph.*, 2(4):217–236, 1983.

[7] E. Bylow, J. Sturm, C. Kerl, F. Kahl, and D. Cremers. Real-time camera tracking and 3d reconstruction using signed distance functions. In *Robotics: Science and Systems*, 2013.

[8] M. Callieri, P. Cignoni, M. Corsini, and R. Scopigno. Masked photo blending: Mapping dense photographic data set on high-resolution sampled 3d models. *Computers & Graphics*, 32(4):464–473, 2008.

[9] F. Crete, T. Dolmiere, P. Ladret, and M. Nicolas. The blur effect: perception and estimation with a new no-reference perceptual blur metric. In *Electronic Imaging*, pages 64920I–64920I–11, 2007.

[10] A. Dai, S. Izadi, and C. Theobalt. Bundlefusion: real-time globally consistent 3d reconstruction using on-the-fly surface re-integration. *Acm Transactions on Graphics*, 36(4):76a, 2017.

[11] L. Do, L. Ma, E. Bondarev, and P. H. N. D. With. On multi-view texture mapping of indoor environments using kinect depth sensors. In *International Conference on Computer Vision Theory and Applications*, pages 739–745, 2015.

[12] M. Eisemann, B. D. Decker, M. Magnor, P. Bekaert, E. D. Aguiar, N. Ahmed, C. Theobalt, and A. Sellent. Floating textures. *Computer Graphics Forum*, 27(2):409C418, 2008.

[13] N. Fioraio, J. Taylor, A. Fitzgibbon, and L. D. Stefano. Large-scale and drift-free surface reconstruction using online subvolume registration. In *CVPR*, 2015.

[14] R. Gal, Y. Wexler, E. Ofek, H. Hoppe, and D. Cohen-Or. Seamless montage for texturing models. *Eurographics 2010*, 29/2, May 2010.

[15] M. Gangnet and A. Blake. Poisson image editing. In *ACM SIGGRAPH*, pages 313–318, 2003.

[16] L. Grammatikopoulos, I. Kalisperakis, G. Karras, and E. Petsa. Automatic multi-view texture mapping of 3d surface projections. pages 12–13, 2007.

[17] M. Halber and T. Funkhouser. Fine-to-coarse global registration of rgb-d scans. In *CVPR*, 2017.

[18] S. Izadi, D. Kim, O. Hilliges, D. Molyneaux, R. Newcombe, P. Kohli, J. Shotton, S. Hodges, D. Freeman, and A. Davison. Kinectfusion:real-time 3d reconstruction and interaction using a moving depth camera. In *ACM Symposium on User Interface Software and Technology, Santa Barbara, Ca, Usa, October*, pages 559–568, 2011.

[19] S. Izadi and M. Stamminger. Real-time 3d reconstruction at scale using voxel hashing. *Acm Transactions on Graphics*, 32(6):169, 2013.

[20] W. Kehl, N. Navab, and S. Ilic. Coloured signed distance fields for full 3d object reconstruction. In *Proceedings of the British Machine Vision Conference*. BMVA Press, 2014.

[21] V. Lempitsky and D. Ivanov. Seamless mosaicing of image-based texture maps. In *CVPR*, pages 1–6, 2007.

[22] R. A. Newcombe, S. Izadi, O. Hilliges, D. Molyneaux, D. Kim, A. J. Davison, P. Kohi, J. Shotton, S. Hodges, and A. Fitzgibbon. Kinectfusion: Real-time dense surface mapping and tracking. In *IEEE International Symposium on Mixed and Augmented Reality*, pages 127–136, 2011.

[23] M. Waechter, N. Moehrle, and M. Goesele. Let there be color! large-scale texturing of 3d reconstructions. In *European Conference on Computer Vision*, pages 836–850, 2014.

[24] W. Wang, J. Shen, and L. Shao. Consistent video saliency using local gradient flow optimization and global refinement. *IEEE Transactions on Image Processing*, 24(11):4185–4196, 2015.

[25] T. Whelan, M. Kaess, H. Johannsson, M. Fallon, J. J. Leonard, and J. Mcdonald. Real-time large-scale dense rgb-d slam with volumetric fusion. *International Journal of Robotics Research*, 34(4-5):598–626, 2015.

[26] T. Whelan, S. Leutenegger, R. S. Moreno, B. Glocker, and A. Davison. Elasticfusion: Dense slam without a pose graph. In *Robotics: Science and Systems*, 2015.

[27] Q. Yan, L. Yang, L. Zhang, and C. Xiao. Distinguishing the indistinguishable: Exploring structural ambiguities via geodesic context. In *CVPR*, pages 3836–3844, 2017.

[28] L. Yang, Q. Yan, Y. Fu, and C. Xiao. Surface reconstruction via fusing sparse-sequence of depth images. *IEEE Transactions on Visualization and Computer Graphics*, 2017.

[29] L. Yang, Q. Yan, and C. Xiao. Shape-controllable geometry completion for point cloud models. *The Visual Computer*, 33(3):385–398, 2017.

[30] Q. Y. Zhou and V. Koltun. Color map optimization for 3d reconstruction with consumer depth cameras. *Acm Transactions on Graphics*, 33(4):1–10, 2014.